www.sciencemag.org/cgi/content/full/science.aav4809/DC1

Supplementary Materials for

Structures and gating mechanism of human TRPM2

Longfei Wang[1,2]*, Tian-Min Fu[1,2]*†, Yiming Zhou[3,4], Shiyu Xia[1,2], Anna Greka[3,4], Hao Wu[1,2]†

*These authors contributed equally to this work.
†Corresponding author. Email: tianmin.fu@childrens.harvard.edu (T.-M.F.); wu@crystal.harvard.edu (H.W.)

Published 22 November 2018 on *Science* First Release
DOI: 10.1126/science.aav4809

This PDF file includes:

Materials and Methods

Expression and purification of full-length human TRPM2 and human and zebrafish NUDT9H domains

Fragments (~1500 bp) of the full-length human TRPM2 gene sequence were synthesized (Quintara Biosciences), PCR amplified to create overlapping ends, and inserted into a BacMam vector with a tobacco etch virus (TEV) protease-cleavable N-terminal MBP tag using the Gibson Assembly Cloning Kit (New England BioLabs). Full-length human TRPM2 was expressed in HEK293F cells using the BacMam method (*39*). Briefly, bacmids encoding human TRPM2 were generated using the Bac-to-Bac method according to the manufacturer's instructions (Thermo Fisher). Sf9 cells cultured in the Hiclone medium were used for production of BacMam baculoviruses. Suspension cultures of HEK293F cells in the Freestyle 293 medium were infected with BacMam baculoviruses at a density of 2×10^6 cells/ml for protein expression. At 24 hrs post-infection, 10 mM sodium butyrate was supplemented into infected cultures to boost protein expression. The cultured cells grew for another 48 hrs at 30 °C before harvesting.

For apo-state TRPM2, HEK293F cells were sonicated and incubated in buffer L (150 mM NaCl, 50 mM HEPES at pH 7.4, 2 mM TCEP, and 2% Glycerol) plus 1% lauryl maltose neopentyl glycol (LMNG), 0.1% cholesteryl hemisuccinate (CHS), and a protease inhibitor cocktail (Sigma-Aldrich). Cell debris was removed by centrifugation at 17,000 rpm for 30 min. Supernatant was incubated with amylose resin (New England BioLabs) for 2 h at 4 °C. The resin was then washed with 10 column volumes of wash buffer (buffer L plus 0.1% LMNG and 0.01% CHS). TRPM2 was eluted with wash buffer plus 20 mM maltose, followed by overnight incubation with TEV protease to remove the MBP tag. TRPM2 was further purified away from MBP using a glycerol gradient. Fractions from the gradient were collected in 250 µl volumes and examined using SDS-PAGE. Fractions containing TRPM2 were pooled and saved for later applications. To prepare for use in electron microscopy, TRPM2 samples was dialyzed against buffer L plus 2 mM EDTA twice, for 4 h and overnight, to remove glycerol and concentrated to desired concentrations.

For primed-state TRPM2, the purification procedure was the same as for apo-state TRPM2 except for the addition of 100 µM ADPR (Sigma-Aldrich) and 2 mM EDTA. For the open-state TRPM2, the cells were sonicated in buffer L plus 100 µM ADPR, 1 mM $CaCl_2$ and the protease inhibitor cocktail, and incubated for 30 min, followed by addition of 1% LMNG and 0.1% CHS and incubation for another 30 min. The remaining purification steps were the same as for apo-state TRPM2 but with the addition of 100 µM ADPR and 1 mM $CaCl_2$ throughout.

Human TRPM2 NUDT9H domain (residues 1228-1503 or 1236-1503) and zebrafish TRPM2 NUDT9H domain (residues 1244-1473) were cloned into the pDB-His-MBP vector to generate constructs with a N-terminal TEV-cleavage MBP tag. The tagged proteins were purified using Ni^{2+}-affinity columns followed by gel filtration chromatography. After MBP removal by TEV, the proteins were further purified by ion exchange chromatography and gel filtration for ADPR hydrolysis and binding assays.

Negative staining electron microscopy

For negative staining, each 2 µl sample containing 0.1 mg/ml TRPM2 was applied on a carbon film grid (CF400-CU, Electron Microscopy Sciences) after plasma glow discharge. The grids were then washed twice with water, stained in 2% uranyl formate for 30 seconds, air dried, and imaged on a Tecnai G2 Spirit BioTWIN microscope (Harvard Medical School Electron Microscopy Facility).

Cryo-EM data collection

For cryo-EM, a sample containing 1 mg/ml TRPM2 was applied on glow discharged Quantinfoil R1.2/1.3 400 mesh copper grids (Electron Microscopy Sciences), blotted for 3.5 seconds in 100% humidity at 4 °C and plunged into liquid ethane using an FEI Vitrobot Mark IV. These grids were screened using either an FEI Talos Arctica microscope (University of Massachusetts Cryo-EM Core Facility) or an FEI F20 microscope (Harvard Cryo-EM Center for Structural Biology). Grids with optimal ice thickness and particle density were chosen for cryo-EM data collection. All data collection was performed using a 300 keV Titan Krios microscope (FEI) equipped with a K2 Summit direct detector (Gatan). For apo-state TRPM2, 2,214 movies were collected in counting mode, with 30 total frames per movie, 70 electrons per $Å^2$ accumulated dose and 0.83 Å physical pixel size. For primed and open states of TRPM2, 1,896 and 1,954 movies were collected respectively in counting mode, with 30 total frames per movie, 70 electrons per $Å^2$ accumulated dose and 1.07 Å pixel size.

Cryo-EM data processing

For all cryo-EM data collected, beam-induced motions were corrected using MotionCor2 (*40*). CTFFIND4 (*41*) was used to determine the defocus value of each micrograph and bad images were excluded manually. For apo-state human TRPM2, 210,091 particles were picked using Gautomatch with no template (http://www.mrc-lmb.cam.ac.uk/kzhang/), extracted and binned for initial 2D classification in RELION (*42*). Particles in good classes were un-binned and subject to a second round of 2D classification using RELION. As a result, 107,815 particles were selected to perform ab initio map reconstruction with C4 symmetry using cisTEM (*43*). The initial model from cisTEM was then low-pass filtered to 60 Å and used as the reference for 3D classification in RELION without applying any symmetry. 34,477 particles from 2 classes were selected for auto-refinement in cisTEM with C4 symmetry. The resulting map has a resolution of 3.6 Å.

Focused refinement was performed on NUDT9H in order to improve map quality. In brief, densities except NUDT9H were subtracted from 34,477 aligned particles, after which 3D classification was performed without alignment. 6,765 full particles from the best NUDT9H class were used for local refinement in cisTEM. The resulting map has improved NUDT9H densities and a resolution of 3.6 Å. To counter orientation preference for side views, particle picking was performed using Gautomatch with only the top view as a template. 291,212 particles were auto-picked, and after two rounds of 2D classification, 82,272 particles were selected for focused refinement of the TM region using the same method as for NUDT9H. The refined map has a resolution of 4.0 Å with traceable densities in the TM region.

For primed-state TRPM2, 132,354 particles were auto-picked using Gautomatch with templates from 2D class averages of apo-state TRPM2. 2D classifications were performed in the same way as for apo-state TRPM2. An *ab initio* map reconstructed

using cisTEM was low-pass filtered and used as the reference for 3D classification in RELION. The final particle set for auto-refinement in cisTEM has 49,383 particles and the primed-state TRPM2 map has a resolution of 6.1 Å.

Image processing of open-state TRPM2 was carried out in the same way as for primed-state TRPM2 except that the reference for 3D classification was low-pass filtered primed-state TRPM2 *ab initio* map. The 3D map was constructed from 26,789 particles to a resolution of 7.2 Å. Focused refinement was performed on the TM region and a subset of 14,199 particles were selected and refined to generate a final 6.4 Å cryo-EM density map. All local resolutions were calculated using ResMap (*44*).

Cryo-EM model building and refinement

The initial homology model of apo-state TRPM2 was created from structures of TRPM4 (PDB ID 6BQR) and NUDT9 (PDB ID 1Q33) using SWISS-MODEL (*45*) and fitted by rigid bodies into the 3.6 Å cryo-EM map using Chimera (*46*). The first round of model refinement was carried out using Rosetta (*47*). The NUDT9H and TM regions were refined against the focused maps with global resolutions of 3.6 Å and 4.0 Å, respectively. Manual adjustments were done using Coot (*48*) and PHENIX (*49*) was used to refine the models against the density maps. The primed-state TRPM2 model was obtained by rigid-body fitting of MHR1/2, NUDT9H and the rest of the apo-state TRPM2 model into the 6.1 Å map. Subsequent refinement was carried out using PHENIX in real space and manual adjustments with Coot. For open-state TRPM2, the TM region model was generated from the apo-state model using Rosetta against the 6.4 Å map. The initial model for cytosolic regions was obtained through rigid body fitting of MHR1/2, MHR3, MHR4 and NUDT9H into the 6.1 Å map and the rest including pole helix and rib helix was directly taken from the apo-state model. Real-space refinements and manual adjustments were then performed. All representations of electron densities and structural models were generated using Chimera and PyMOL (*50*).

Binding affinity measurements

For surface plasmon resonance (SPR) assay, recombinant human TRPM2 and human NUDT9H were immobilized to the CM5 sensor chip (GE Healthcare) as previously described (*51*). The first channel with no immobilized protein was used as a reference channel. After injection of ADPR at various concentrations, changes of responses in sensorgrams were measured. The running buffer contains 20 mM HEPES (pH 7.4), 150 mM NaCl, and 0.05% Tween 20. All experiments were performed on a Biacore T200 (GE Healthcare) at 25°C. Curve fitting was carried out using the BIAevaluation and Prism software suit.

For microscale thermophoresis (MST) assay, the binding affinity between recombinant NUDT9H and ADPR was measured at 25°C in a binding buffer containing 20 mM HEPES at pH 7.4, 150 mM NaCl and 0.05% Tween 20 using MONOLITH NT.115pico (NanoTemper Technologies). NUDT9H proteins were labeled using the red fluorescent dye NT-647 according to the standard protocol from the labeling kit (NanoTemper Technologies). The labeled NUDT9H proteins were diluted 500-fold and mixed 1:1 (v/v) with ADPR serial dilutions. The data were analyzed using the MO.Affinity (NanoTemper Technologies).

ADPR hydrolysis assay

Hydrolytic activities of purified full-length human TRPM2 and NUDT9H constructs were assessed using thin layer chromatography (TLC) based on a previously reported protocol (*5*). Mixtures containing 1 μM proteins and 10 mM ADPR in reaction buffer (50 mM HEPES at pH 7.5, 150 mM NaCl, 16 mM $MgCl_2$) were incubated at 25 or 37 °C for 20 min. Recombinant human mitochondrial NUDT9 (Novus Biologicals) was used as a positive control. Reactions were quenched on ice, and 1 μL aliquots of reaction mixtures were added to TLC sheets coated with 0.2 mm silica gel (sMacherey-Nagel). The TLC sheets were then placed in a sealed glass chamber containing the developing buffer (0.2 M NH_4HCO_3 and 70% ethanol) for 20 min, air dried, and imaged under UV light for the detection of ADPR and the hydrolytic product AMP.

Ca^{2+} imaging and electrophysiology

HEK293T cells were maintained in Dulbecco's modified Eagle's medium (DMEM) containing 10% heat-inactivated fetal bovine serum (FBS), 100 units/ml penicillin and streptomycin, and 2 mM L-glutamine in a 5% CO_2 incubator at 37 °C. The cells were co-transfected by 1 μg human wild-type TRPM2 or NUDT9H-deleted plasmids with 0.1 μg mCherry or GFP plasmids using the Lipofectamine 2000 reagent following a recommended protocol (Life Technologies, Thermo Fisher Scientific). These transfected cells were used for Ca^{2+} imaging and electrophysiology experiments.

Intracellular Ca^{2+} imaging was performed in the presence of 5 μM Fura-2 AM, a ratiometric calcium indicator (Invitrogen, Thermo Fisher Scientific) 16 h after transfection. The extracellular solution contained 140 mM NaCl, 5 mM KCl, 2 mM $MgCl_2$, 2 mM $CaCl_2$, 10 mM Glucose, 100 μM ADPR and 10 mM HEPES at pH 7.4 adjusted with NaOH. Cells were excited at 340 nm and 380 nm and the emission was monitored at 510 nm using a CCD camera (Hamamatsu Photonics) after incubation with Fura-2 AM for 30 minutes. Data were acquired and analyzed using the Metafluor software (Molecular Devices).

Outside-out single-channel patch clamp experiments were performed at 16 to 24 h after TRPM2 transfection. The standard bath solution was the same as that for Ca^{2+} imaging experiments, except for the calcium-free bath solution where we replaced 2 mM $CaCl_2$ with 5 mM EGTA. The pipette solutions contained 140 mM CsAspartate, 10 mM CsCl, 1 mM $MgCl_2$, 0.5 mM EGTA, 10 mM mannitol, and 10 mM HEPES at pH 7.4 adjusted with CsOH. The pipette solutions were freshly prepared in the presence or absence of 1 μM ADPR. Membrane potential was clamped at -60 mV. Single-channel data were sampled at 10 kHz and filtered at 2 kHz using the Axon 200B and Digidata 1550A. Data were recorded using pClamp 10.6 and analyzed using the Clampfit 10.6 software.

Cellular imaging

Wild-type and NUDT9H-deleted TRPM2 constructs were transiently transfected into HEK293T cells. At 20 h post-transfection, cells were stained by Hoechst for 1 h for nucleus staining. Afterwards, the cells were fixed by 4% paraformaldehyde in PBS for 5 min and then washed twice using PBS. Fixed cells were incubated for 90 min with anti-TRPM2 primary antibody (Abcam ab11168) in PBS plus 30 mg/ml BSA followed by three PBS washes. Secondary antibody conjugated with alexa fluor-488 was incubated

with the cells for another 60 min and residual dye removed by three PBS washes. All images were taken under an Olympus FluoView FV1000 confocal microscope.

Statistical analysis

Group data represent the Mean ± SEM. Statistical analysis was performed with Student's t-test or one-way ANOVA following Bonferroni's *post hoc* analysis using the GraphPad Prism 6 software. $P < 0.05$ was considered to be significant.

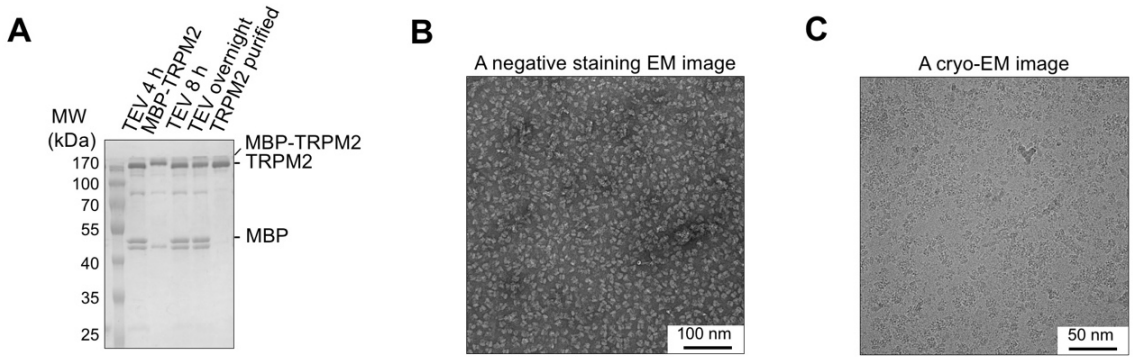

Fig. S1.
Purification of human TRPM2. (**A**) SDS-PAGE showing the fractions collected at each step during the purification of *hs*TRPM2. (**B-C**) Representative negative staining (B) and cryo-EM (C) micrographs of apo *hs*TRPM2. Scale bars: 100 nm and 50 nm, respectively.

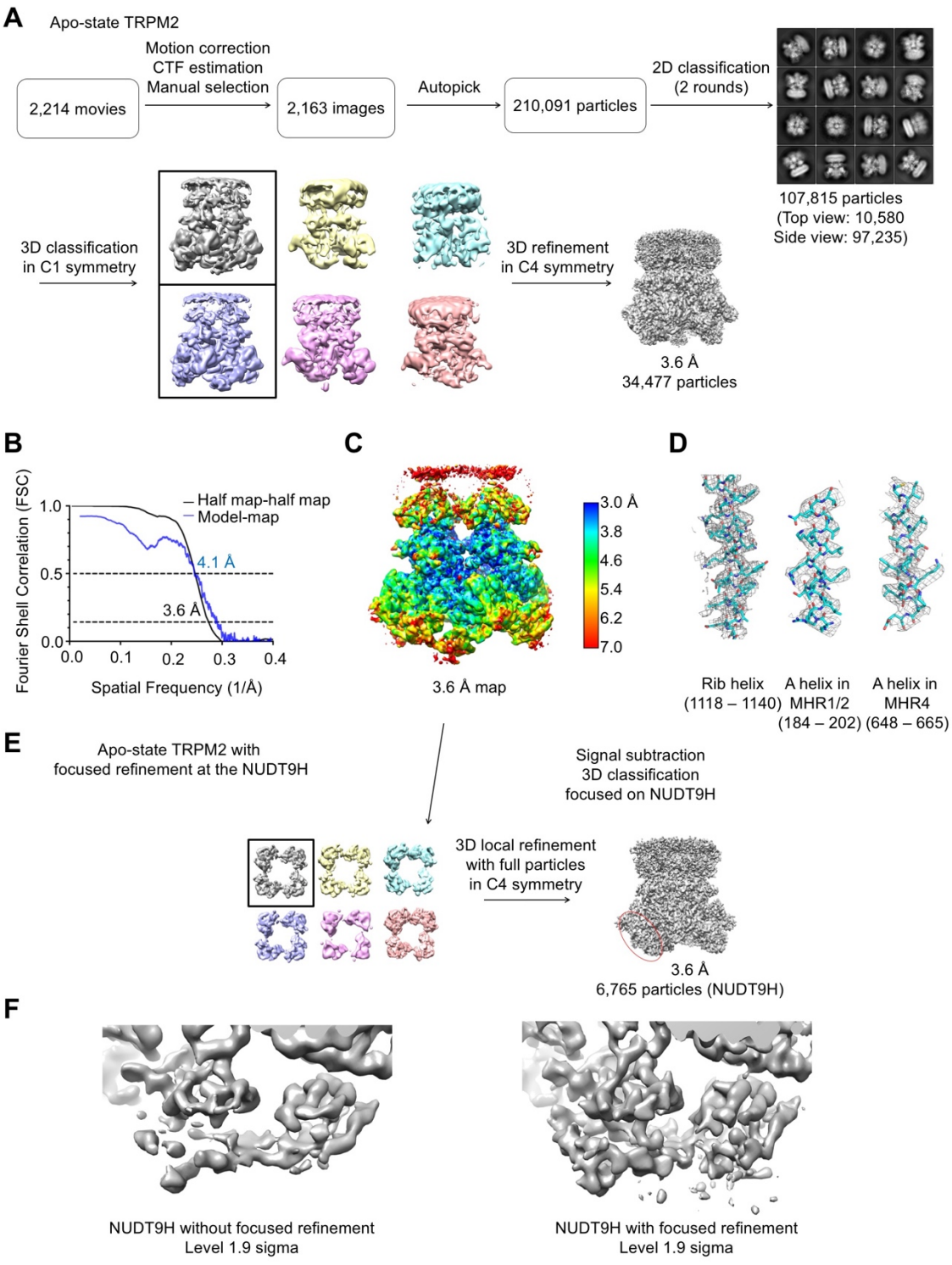

Fig. S2.

3D reconstruction of human TRPM2 in the apo state. (**A**) Workflow of 3D reconstruction of *hs*TRPM2 in the apo state. (**B**) FSC curves for the 3D reconstruction of apo-state *hs*TRPM2. (**C**) Local resolution map of the reconstruction. The resolution is color-coded as indicated by the scale bar. (**D**) Representative segments of the cryo-EM

density map fitted with the final atomic model. (**E**) Focused refinement at the NUDT9H region. (**F**) Comparison of the NUDT9H domain density with and without focused refinement.

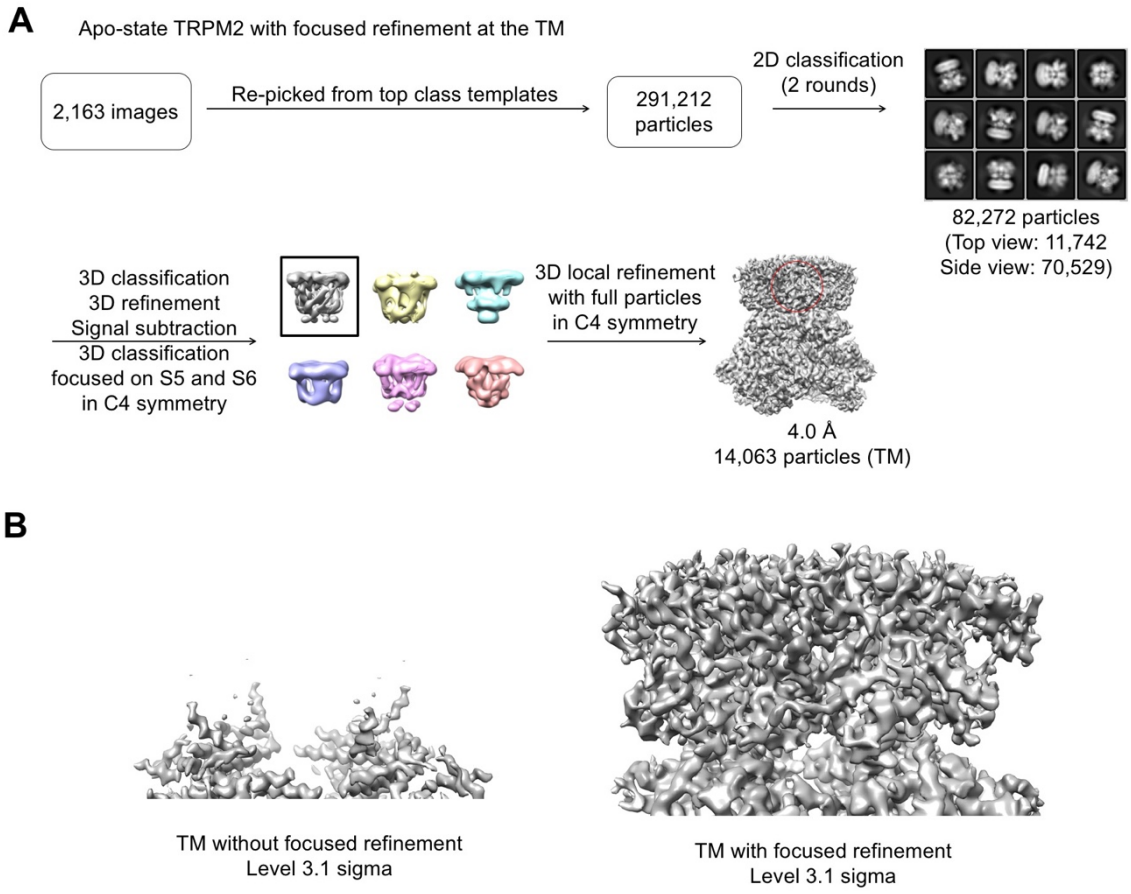

Fig. S3.
Focused 3D reconstruction of the transmembrane (TM) region of human TRPM2 in the apo state. (**A**) Workflow of focused 3D reconstruction of apo hsTRPM2 at the TM region. (**B**) Comparison of the TM domain density with and without focused refinement.

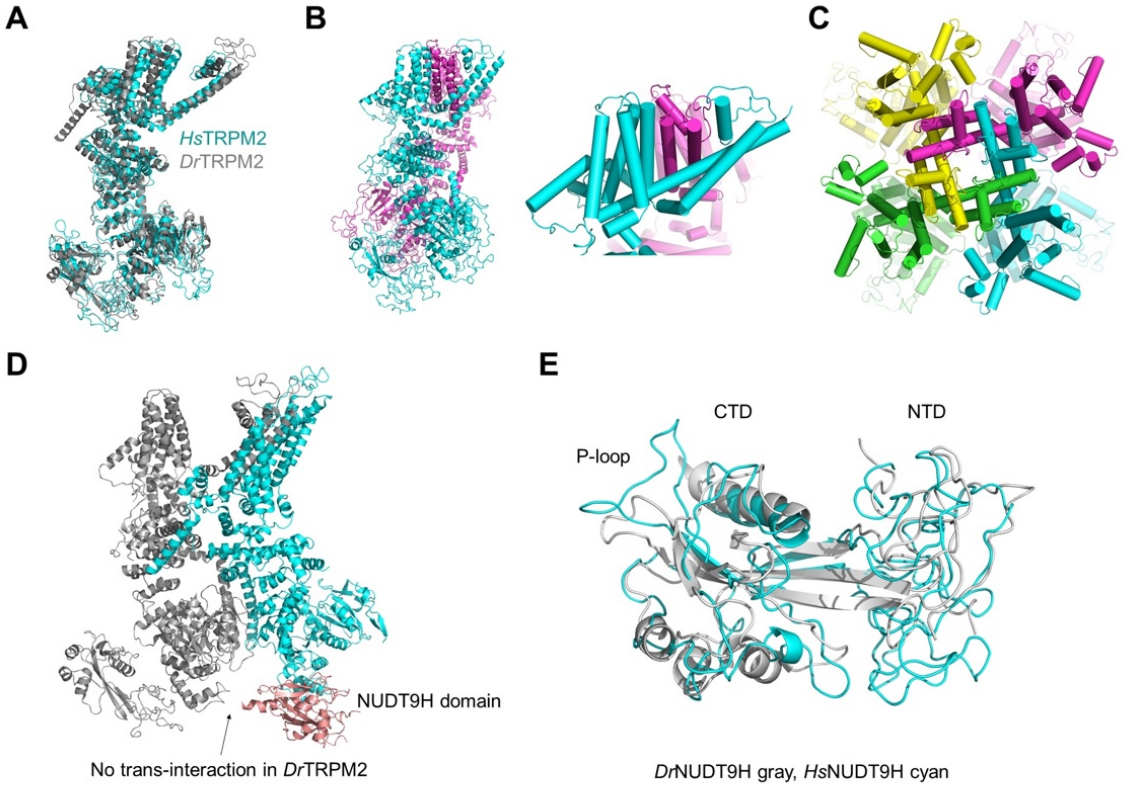
A
HsTRPM2
DrTRPM2
B
C
D
NUDT9H domain
No trans-interaction in DrTRPM2
E
CTD
NTD
P-loop
DrNUDT9H gray, HsNUDT9H cyan

F

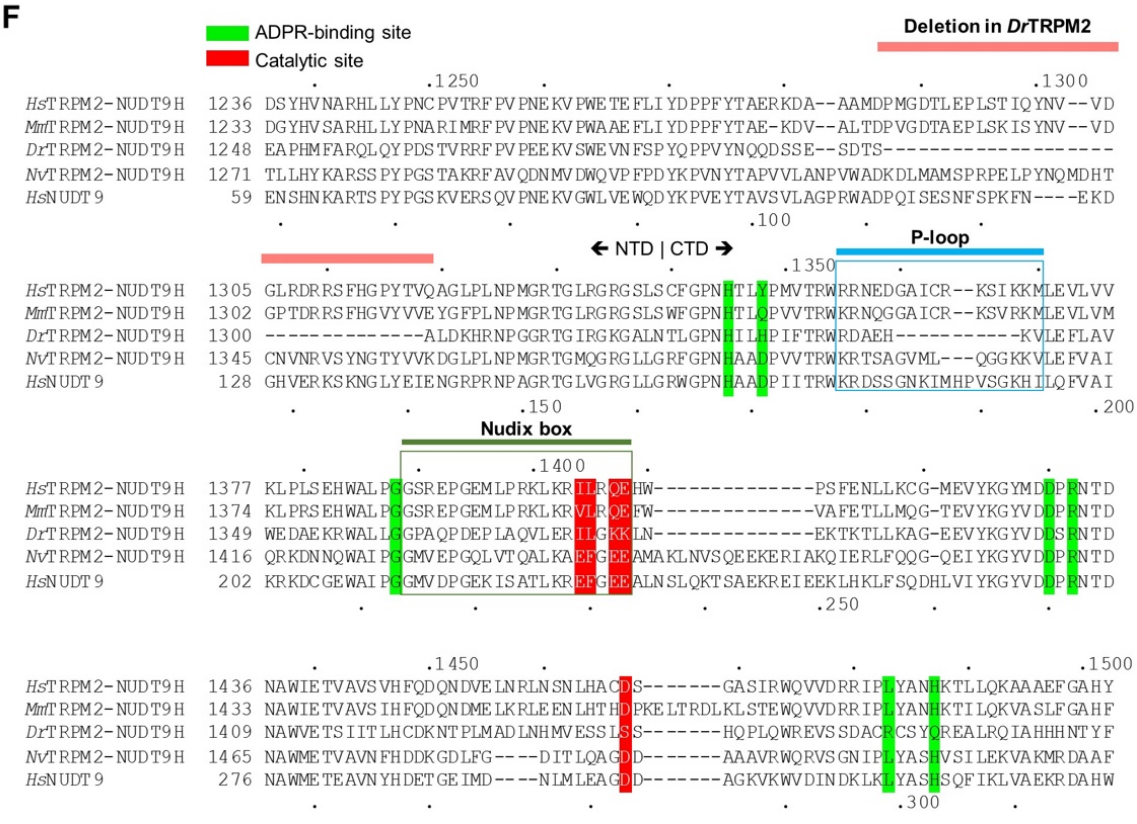
ADPR-binding site
Catalytic site
Deletion in DrTRPM2
← NTD | CTD →
P-loop
Nudix box
HsTRPM2-NUDT9H
MmTRPM2-NUDT9H
DrTRPM2-NUDT9H
NvTRPM2-NUDT9H
HsNUDT9

Fig. S4.
Structure of human TRPM2 in the apo state and its comparison with *dr*TRPM2. (**A**) Structural comparison between apo *hs*TRPM2 (cyan) and *dr*TRPM2 (gray). **(B-C)** Domain-swapped architecture of the TM region of *hs*TRPM2, where helices S1-S4 interact with the S5-S6 pore domain of an adjacent subunit, demonstrated with two subunits (B) and the tetramer structure of *hs*TRPM2 (C). **(D)** Structure of *dr*TRPM2 in apo state, two subunits shown. **(E)** Structural comparison of the NUDT9H domain in *hs*TRPM2 and *dr*TRPM2. **(F)** Multiple sequence alignment of NUDT9H domains in TRPM2 across species.

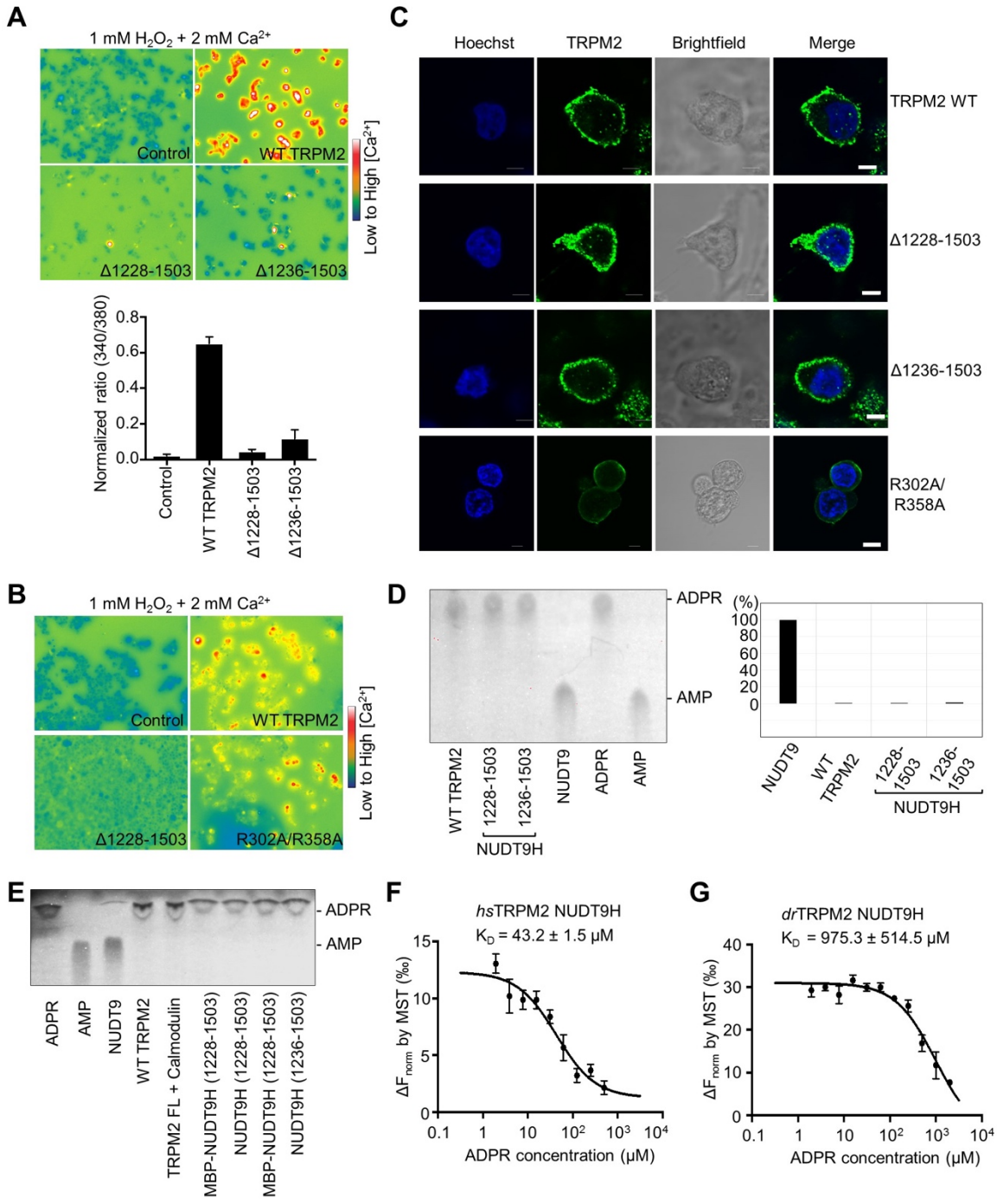

Fig. S5.

ADPR binding and channel gating. (**A**) Ca^{2+} imaging and statistical analysis of HEK293T cells expressing wild-type and NUDT9H-deleted TRPM2 in response to 1 mM H_2O_2. (**B**) Ca^{2+} imaging of HEK293T cells expressing wild-type and R302A/R358A mutant TRPM2 in response to 1 mM H_2O_2. (**C**) Cell-surface expression of wild-type TRPM2, NUDT9H-deleted, and R302A/R358A mutant TRPM2 constructs in HEK293T cells. (**D**) ADPR hydrolase activity of full-length TRPM2, NUDT9H, and NUDT9

assessed by thin layer chromatography at room temperature (left) and quantification of the activity (right). (**E**) ADPR hydrolase activity of full-length TRPM2, NUDT9H, and NUDT9 assessed by thin layer chromatography at 37°C. (**F**) ADPR-binding affinity of *hs*TRPM2 NUDT9H measured by microscale thermophoresis (MST). (**G**) ADPR-binding affinity of *dr*TRPM2 NUDT9H measured by MST.

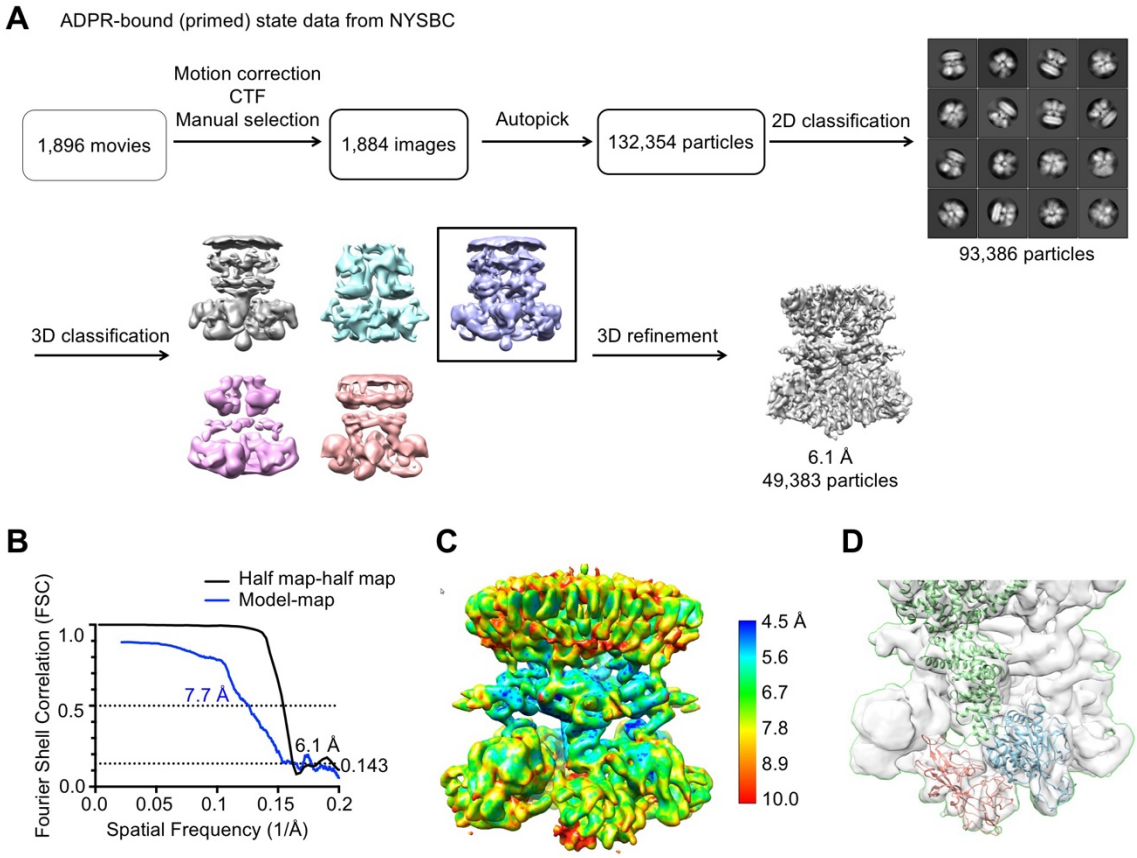

Fig. S6.

3D reconstruction of human TRPM2 in the primed state. (**A**) Workflow of 3D reconstruction of *hs*TRPM2 in the ADPR-bound state. (**B**) FSC curves for the reconstruction of primed *hs*TRPM2. (**C**) Local resolution map of the reconstruction. The resolution is color-coded as indicated by the scale bar. (**D**) Model fitting into the cryo-EM density of ADPR-bound *hs*TRPM2.

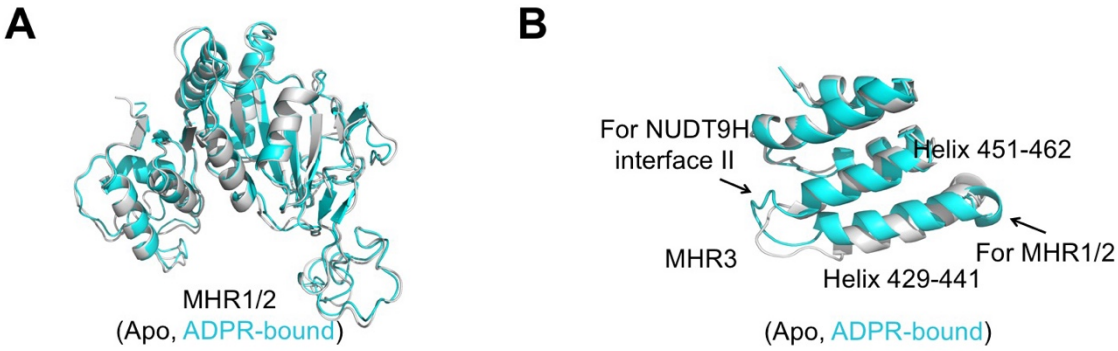

Fig. S7.
Structural comparison between apo and ADPR-bound TRPM2. (A) Overlay of MHR1/2 in the ADPR-bound (cyan) and apo (gray) states, showing that the domain structures do not change significantly. (**B**) Overlay of MHR3 in the ADPR-bound (cyan) and apo (gray) states, showing conformational changes at the helical hairpin. Regions for contacting NUDT9H and MHR1/2 are indicated.

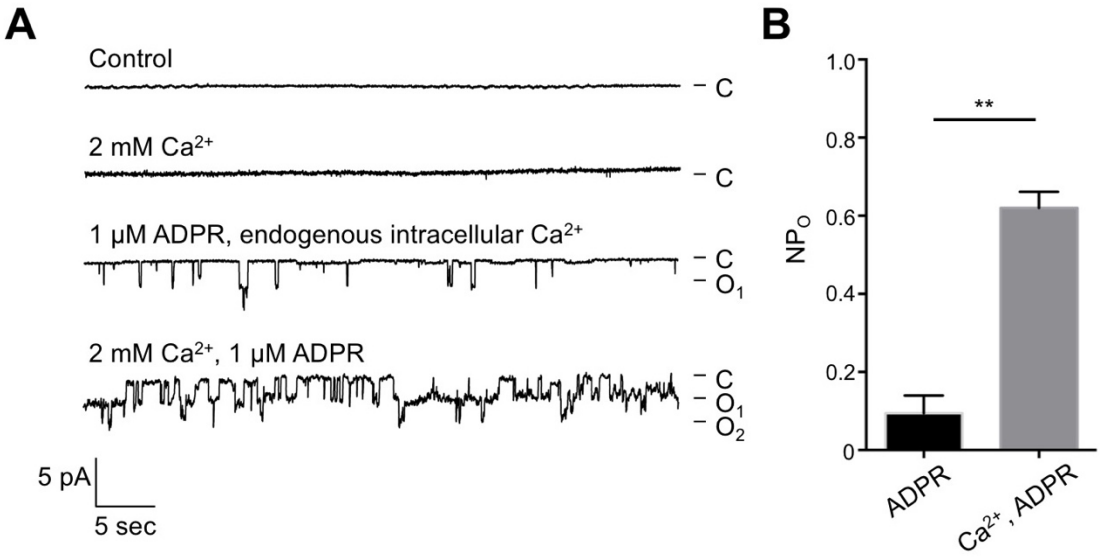

Fig. S8.

Single-channel recording of HEK293T cells expressing human TRPM2. (**A**) Single-channel currents of *hs*TRPM2 in response to 1 μM ADPR with or without extracellular Ca^{2+}. Control: pipette solution with no ADPR and no extracellular Ca^{2+}; 2 mM Ca^{2+}: bath solutions with 2 mM extracellular Ca^{2+}; 1 μM ADPR: pipette solution with 1 μM ADPR; 1 μM ADPR + 2 mM Ca^{2+}: pipette solution with 1 μM ADPR and 2 mM extracellular Ca^{2+}. C: closed state; O_1: open state 1; O_2: open state 2, which may represent two channels opening at the same time. Membrane potential was kept at -60 mV. (**B**) The total open-state probability (NP_o) of *hs*TRPM2 in response to 1 μM ADPR with or without extracellular Ca^{2+}. **$P < 0.01$. Mean ± SEM. n = 3 for each group.

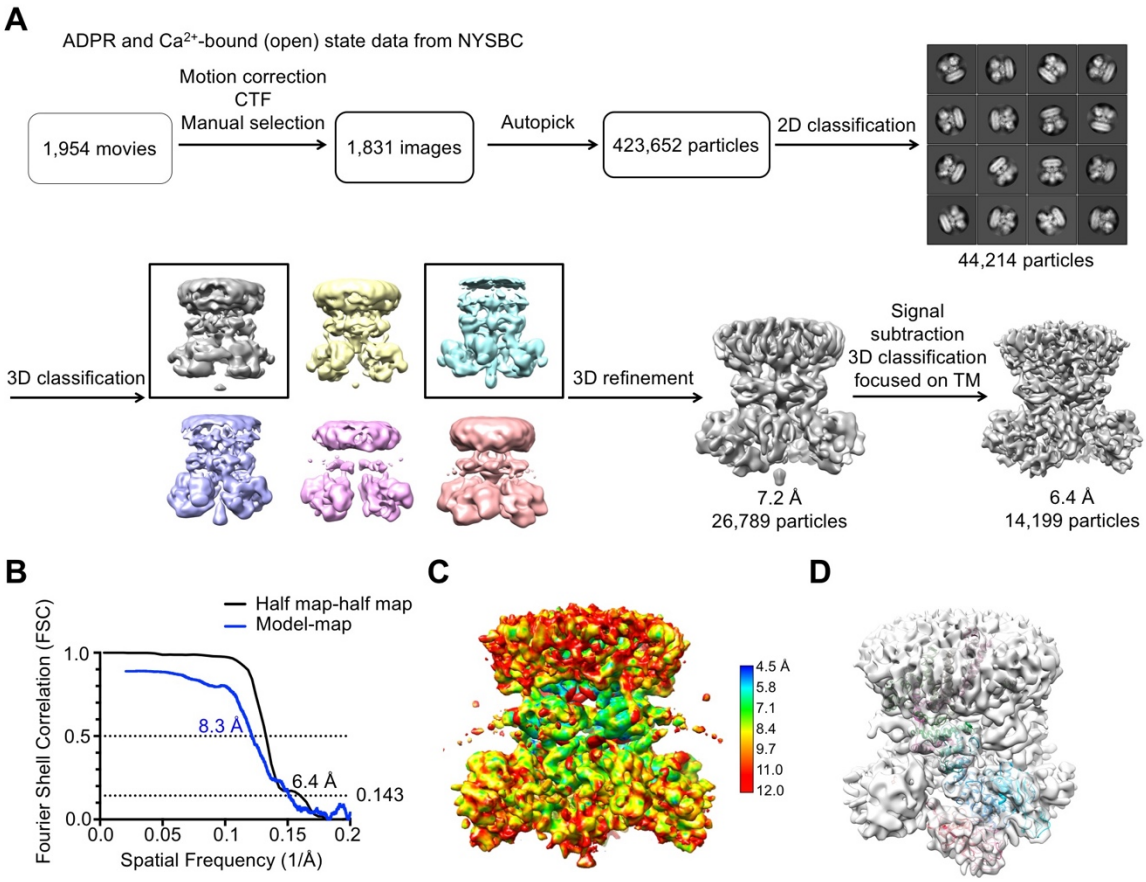

Fig. S9.

3D reconstruction of human TRPM2 in the open state. (**A**) Workflow of 3D reconstruction of *hs*TRPM2 in the open state. (**B**) FSC curves for the reconstruction. (**C**) Local resolution map of the reconstruction. The resolution is color-coded as indicated by the scale bar. (**D**) Model fitting into the cryo-EM density of open-state *hs*TRPM2.

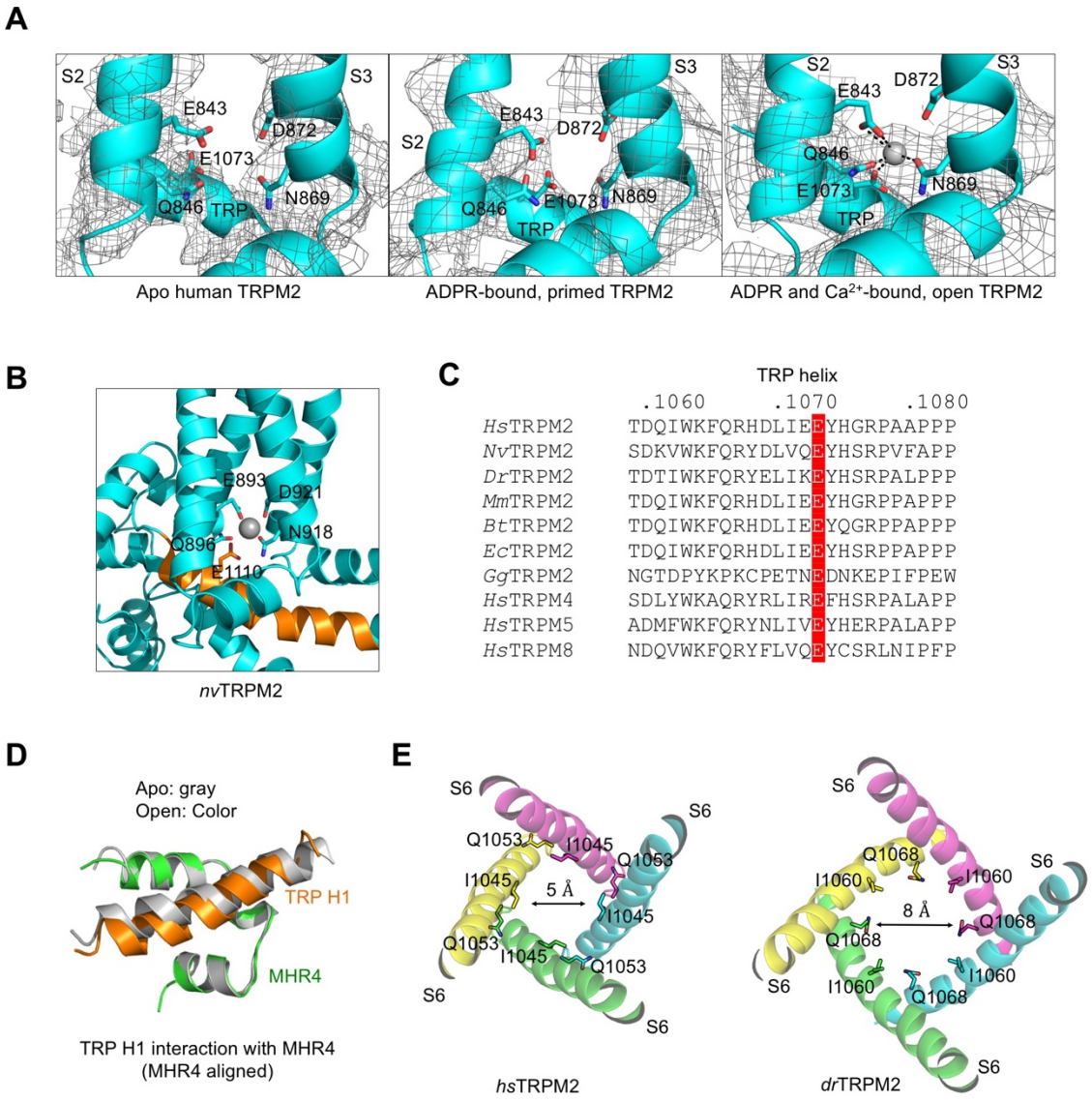

Fig. S10.

Calcium-binding site in TRPM2. (A) cryo-EM density comparison of key residues at the Ca^{2+}-binding site in *hs*TRPM2 structures in apo, primed, and open states. **(B)** Ca^{2+}-binding site of *nv*TRPM2. **(C)** Sequence alignment of TRP H1 from TRPM2 of different species, *hs*TRPM4, *hs*TRPM5, and *hs*TRPM8. **(D)** TRP H1 and MHR4 are rigidly coupled, shown as a local superposition between the apo (gray) and open (colored) states. (**E**) Comparison of the lower gating pores in *hs*TRPM2 and *dr*TPRM2.

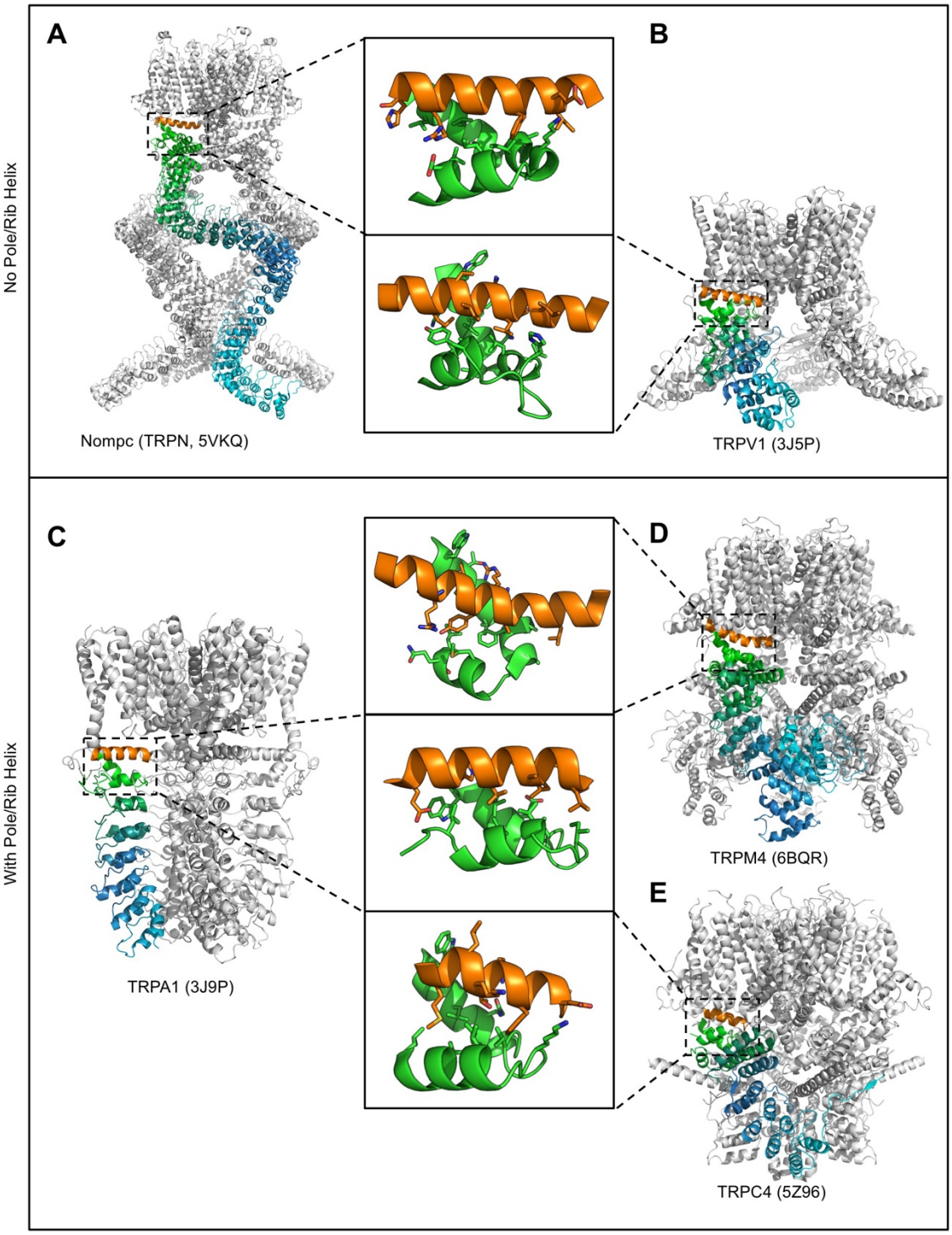

Fig. S11.
Coupling of TRP H1 to cytosolic domains in various TRP channels. **(A)** Fruit fly NOMPC (PDB ID: 5VKQ). **(B)** Rat TRPV1 (PDB ID: 3J5P). **(C)** Human TRPA1 (PDB ID: 3J9P). **(D)** Human TRPM4 (PDB ID: 6BQR). **(E)** Mouse TRPC4 (PDB ID: 5Z96).

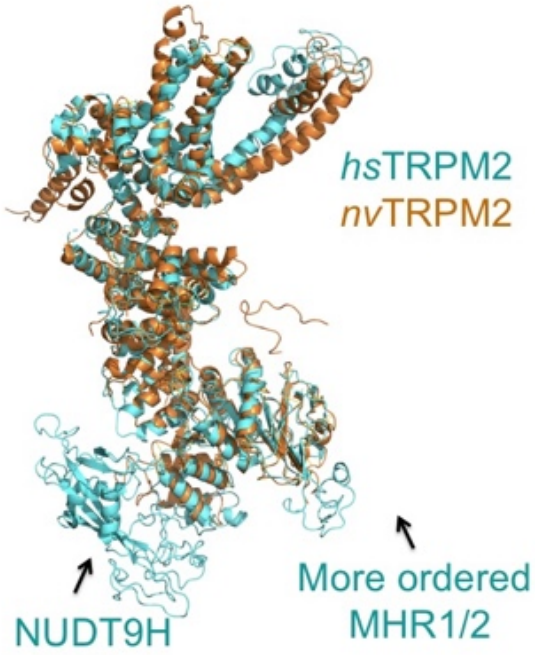

Fig. S12.
Structural overlay of apo *hs*TRPM2 (cyan) and Ca^{2+}-bound *nv*TRPM2 (orange).

Table S1.
Cryo-EM data collection, refinement, and validation statistics.

	Apo - NYSBC (EMD-9132) (PDB 6MIX)	Primed - NYSBC (EMD-9133) (PDB 6MIZ)	Open - NYSBC (EMD-9134) (PDB 6MJ2)
Data collection & processing			
Magnification	29,000	22,500	22,500
Voltage (keV)	300	300	300
Electron exposure (e/Å^2)	70.12	70.072	70.072
Defocus range (μm)	1.0 - 2.0	1.0 - 2.0	1.0 - 2.0
Pixel size (Å)	0.832	1.07	1.07
Symmetry imposed	C4	C4	C4
Initial particles (no.)	210,091	132,354	423,652
Final particles (no.)	34,477	49,383	14,199
Map resolution (Å)	3.6	6.1	6.4
FSC threshold	0.143	0.143	0.143
Refinement			
Initial model (PDB code)	6BQR	6MIX	6MIX
Model resolution (Å)	4.07	7.7	8.3
FSC threshold	0.5	0.5	0.5
Model resolution range (Å)	99.3 - 4.07	99.3 - 7.7	99.3 - 8.3
Map sharpening *B* factor (Å^2)	-90.00	-520.03	-421.48.00
Model composition			
Non-hydrogen atoms	43,116	43,116	43,116
Protein residues	5,348	5,348	5,348
Ligands	N/A	N/A	4
R.m.s. deviations			
Bond lengths (Å)	0.008	0.006	0.006
Bond angles (°)	1.314	1.334	1.226
Validation			
MolProbity score	2.38	2.24	2.33
Clash score	14.53	11.71	13.49
Poor rotamers (%)	0.51	0.34	0.26
Ramachandran plot			
Favored (%)	81.88	85.04	83.21
Allowed (%)	17.85	14.58	16.41
Disallowed (%)	0.38	0.38	0.38

References and Notes

1. D. E. Clapham, TRP channels as cellular sensors. *Nature* **426**, 517–524 (2003). doi:10.1038/nature02196 Medline

2. K. Venkatachalam, C. Montell, TRP channels. *Annu. Rev. Biochem.* **76**, 387–417 (2007). doi:10.1146/annurev.biochem.75.103004.142819 Medline

3. D. Julius, TRP channels and pain. *Annu. Rev. Cell Dev. Biol.* **29**, 355–384 (2013). doi:10.1146/annurev-cellbio-101011-155833 Medline

4. B. Tóth, I. Iordanov, L. Csanády, Putative chanzyme activity of TRPM2 cation channel is unrelated to pore gating. *Proc. Natl. Acad. Sci. U.S.A.* **111**, 16949–16954 (2014). doi:10.1073/pnas.1412449111 Medline

5. I. Iordanov, C. Mihályi, B. Tóth, L. Csanády, The proposed channel-enzyme transient receptor potential melastatin 2 does not possess ADP ribose hydrolase activity. *eLife* **5**, e17600 (2016). doi:10.7554/eLife.17600 Medline

6. K. Nagamine, J. Kudoh, S. Minoshima, K. Kawasaki, S. Asakawa, F. Ito, N. Shimizu, Molecular cloning of a novel putative Ca^{2+} channel protein (TRPC7) highly expressed in brain. *Genomics* **54**, 124–131 (1998). doi:10.1006/geno.1998.5551 Medline

7. A. L. Perraud, A. Fleig, C. A. Dunn, L. A. Bagley, P. Launay, C. Schmitz, A. J. Stokes, Q. Zhu, M. J. Bessman, R. Penner, J.-P. Kinet, A. M. Scharenberg, ADP-ribose gating of the calcium-permeable LTRPC2 channel revealed by Nudix motif homology. *Nature* **411**, 595–599 (2001). doi:10.1038/35079100 Medline

8. Y. Sano, K. Inamura, A. Miyake, S. Mochizuki, H. Yokoi, H. Matsushime, K. Furuichi, Immunocyte Ca^{2+} influx system mediated by LTRPC2. *Science* **293**, 1327–1330 (2001). doi:10.1126/science.1062473 Medline

9. L. Csanády, B. Törocsik, Four Ca^{2+} ions activate TRPM2 channels by binding in deep crevices near the pore but intracellularly of the gate. *J. Gen. Physiol.* **133**, 189–203 (2009). doi:10.1085/jgp.200810109 Medline

10. K. Uchida, M. Tominaga, TRPM2 modulates insulin secretion in pancreatic β-cells. *Islets* **3**, 209–211 (2011). doi:10.4161/isl.3.4.16130 Medline

11. K. Song, H. Wang, G. B. Kamm, J. Pohle, F. C. Reis, P. Heppenstall, H. Wende, J. Siemens, The TRPM2 channel is a hypothalamic heat sensor that limits fever and can drive hypothermia. *Science* **353**, 1393–1398 (2016). doi:10.1126/science.aaf7537 Medline

12. C. H. Tan, P. A. McNaughton, The TRPM2 ion channel is required for sensitivity to warmth. *Nature* **536**, 460–463 (2016). doi:10.1038/nature19074 Medline

13. A. L. Perraud, C. L. Takanishi, B. Shen, S. Kang, M. K. Smith, C. Schmitz, H. M. Knowles, D. Ferraris, W. Li, J. Zhang, B. L. Stoddard, A. M. Scharenberg, Accumulation of free ADP-ribose from mitochondria mediates oxidative stress-induced gating of TRPM2 cation channels. *J. Biol. Chem.* **280**, 6138–6148 (2005). doi:10.1074/jbc.M411446200 Medline

14. S. Yamamoto, S. Shimizu, S. Kiyonaka, N. Takahashi, T. Wajima, Y. Hara, T. Negoro, T. Hiroi, Y. Kiuchi, T. Okada, S. Kaneko, I. Lange, A. Fleig, R. Penner, M. Nishi, H.

Takeshima, Y. Mori, TRPM2-mediated Ca^{2+} influx induces chemokine production in monocytes that aggravates inflammatory neutrophil infiltration. *Nat. Med.* **14**, 738–747 (2008). doi:10.1038/nm1758 Medline

15. H. Knowles, J. W. Heizer, Y. Li, K. Chapman, C. A. Ogden, K. Andreasen, E. Shapland, G. Kucera, J. Mogan, J. Humann, L. L. Lenz, A. D. Morrison, A.-L. Perraud, Transient receptor potential melastatin 2 (TRPM2) ion channel is required for innate immunity against *Listeria monocytogenes*. *Proc. Natl. Acad. Sci. U.S.A.* **108**, 11578–11583 (2011). doi:10.1073/pnas.1010678108 Medline

16. J. K. Tripathi, A. Sharma, P. Sukumaran, Y. Sun, B. B. Mishra, B. B. Singh, J. Sharma, Oxidant sensor cation channel TRPM2 regulates neutrophil extracellular trap formation and protects against pneumoseptic bacterial infection. *FASEB J.* 10.1096/fj.201800605 (2018).

17. N. L. Shakerley, A. Chandrasekaran, M. Trebak, B. A. Miller, J. A. Melendez, *Francisella tularensis* catalase restricts immune function by impairing TRPM2 Channel activity. *J. Biol. Chem.* **291**, 3871–3881 (2016). doi:10.1074/jbc.M115.706879 Medline

18. Z. Zhong, Y. Zhai, S. Liang, Y. Mori, R. Han, F. S. Sutterwala, L. Qiao, TRPM2 links oxidative stress to NLRP3 inflammasome activation. *Nat. Commun.* **4**, 1611 (2013). doi:10.1038/ncomms2608 Medline

19. S. Yamamoto, S. Shimizu, Significance of TRP channels in oxidative stress. *Eur. J. Pharmacol.* **793**, 109–111 (2016). doi:10.1016/j.ejphar.2016.11.007 Medline

20. V. G. Ostapchenko, M. Chen, M. S. Guzman, Y.-F. Xie, N. Lavine, J. Fan, F. H. Beraldo, A. C. Martyn, J. C. Belrose, Y. Mori, J. F. MacDonald, V. F. Prado, M. A. M. Prado, M. F. Jackson, The transient receptor potential melastatin 2 (TRPM2) channel contributes to β-amyloid oligomer-related neurotoxicity and memory impairment. *J. Neurosci.* **35**, 15157–15169 (2015). doi:10.1523/JNEUROSCI.4081-14.2015 Medline

21. H. E. Autzen, A. G. Myasnikov, M. G. Campbell, D. Asarnow, D. Julius, Y. Cheng, Structure of the human TRPM4 ion channel in a lipid nanodisc. *Science* **359**, 228–232 (2018). doi:10.1126/science.aar4510 Medline

22. J. Guo, J. She, W. Zeng, Q. Chen, X. C. Bai, Y. Jiang, Structures of the calcium-activated, non-selective cation channel TRPM4. *Nature* **552**, 205–209 (2017). Medline

23. P. A. Winkler, Y. Huang, W. Sun, J. Du, W. Lü, Electron cryo-microscopy structure of a human TRPM4 channel. *Nature* **552**, 200–204 (2017). Medline

24. J. Duan, Z. Li, J. Li, A. Santa-Cruz, S. Sanchez-Martinez, J. Zhang, D. E. Clapham, Structure of full-length human TRPM4. *Proc. Natl. Acad. Sci. U.S.A.* **115**, 2377–2382 (2018). doi:10.1073/pnas.1722038115 Medline

25. Y. Yin, M. Wu, L. Zubcevic, W. F. Borschel, G. C. Lander, S.-Y. Lee, Structure of the cold- and menthol-sensing ion channel TRPM8. *Science* **359**, 237–241 (2018). doi:10.1126/science.aan4325 Medline

26. Z. Zhang, B. Tóth, A. Szollosi, J. Chen, L. Csanády, Structure of a TRPM2 channel in complex with Ca^{2+} explains unique gating regulation. *eLife* **7**, e36409 (2018). doi:10.7554/eLife.36409 Medline

27. J. Duan, Z. Li, J. Li, R. E. Hulse, A. Santa-Cruz, W. C. Valinsky, S. A. Abiria, G. Krapivinsky, J. Zhang, D. E. Clapham, Structure of the mammalian TRPM7, a magnesium channel required during embryonic development. *Proc. Natl. Acad. Sci. U.S.A.* **115**, E8201–E8210 (2018). doi:10.1073/pnas.1810719115 Medline

28. Y. Huang, P. A. Winkler, W. Sun, W. Lü, J. Du, Architecture of the TRPM2 channel and its activation mechanism by ADP-ribose and calcium. *Nature* **562**, 145–149 (2018). doi:10.1038/s41586-018-0558-4 Medline

29. B. W. Shen, A. L. Perraud, A. Scharenberg, B. L. Stoddard, The crystal structure and mutational analysis of human NUDT9. *J. Mol. Biol.* **332**, 385–398 (2003). doi:10.1016/S0022-2836(03)00954-9 Medline

30. P. Yu, X. Xue, J. Zhang, X. Hu, Y. Wu, L.-H. Jiang, H. Jin, J. Luo, L. Zhang, Z. Liu, W. Yang, Identification of the ADPR binding pocket in the NUDT9 homology domain of TRPM2. *J. Gen. Physiol.* **149**, 219–235 (2017). doi:10.1085/jgp.201611675 Medline

31. R. Fliegert, A. Bauche, A.-M. Wolf Pérez, J. M. Watt, M. D. Rozewitz, R. Winzer, M. Janus, F. Gu, A. Rosche, A. Harneit, M. Flato, C. Moreau, T. Kirchberger, V. Wolters, B. V. L. Potter, A. H. Guse, 2′-Deoxyadenosine 5′-diphosphoribose is an endogenous TRPM2 superagonist. *Nat. Chem. Biol.* **13**, 1036–1044 (2017). doi:10.1038/nchembio.2415 Medline

32. J. Starkus, A. Beck, A. Fleig, R. Penner, Regulation of TRPM2 by extra- and intracellular calcium. *J. Gen. Physiol.* **130**, 427–440 (2007). doi:10.1085/jgp.200709836 Medline

33. L. L. McGoldrick, A. K. Singh, K. Saotome, M. V. Yelshanskaya, E. C. Twomey, R. A. Grassucci, A. I. Sobolevsky, Opening of the human epithelial calcium channel TRPV6. *Nature* **553**, 233–237 (2018). doi:10.1038/nature25182 Medline

34. A. K. Singh, L. L. McGoldrick, A. I. Sobolevsky, Structure and gating mechanism of the transient receptor potential channel TRPV3. *Nat. Struct. Mol. Biol.* **25**, 805–813 (2018). doi:10.1038/s41594-018-0108-7 Medline

35. W. A. Catterall, G. Wisedchaisri, N. Zheng, The chemical basis for electrical signaling. *Nat. Chem. Biol.* **13**, 455–463 (2017). doi:10.1038/nchembio.2353 Medline

36. H. Nam Tran, J. Hederih, T. Numata, M. X. Mori, S. Maegawa, H. Hosokawa, Y. Mori, Functional charaterization of zebrafish transient receptor potential melastatin 2. *Biophys. J.* **114**, 641A–642A (2018). doi:10.1016/j.bpj.2017.11.3463

37. F. Kühn, C. Kühn, A. Lückhoff, Different principles of ADP-ribose-mediated activation and opposite roles of the NUDT9 homology domain in the TRPM2 orthologs of man and sea anemone. *Front. Physiol.* **8**, 879 (2017). doi:10.3389/fphys.2017.00879 Medline

38. O. S. Smart, J. G. Neduvelil, X. Wang, B. A. Wallace, M. S. Sansom, HOLE: A program for the analysis of the pore dimensions of ion channel structural models. *J. Mol. Graph.* **14**, 354–360, 376 (1996). doi:10.1016/S0263-7855(97)00009-X Medline

39. A. Dukkipati, H. H. Park, D. Waghray, S. Fischer, K. C. Garcia, BacMam system for high-level expression of recombinant soluble and membrane glycoproteins for structural studies. *Protein Expr. Purif.* **62**, 160–170 (2008). doi:10.1016/j.pep.2008.08.004 Medline

40. S. Q. Zheng, E. Palovcak, J. P. Armache, K. A. Verba, Y. Cheng, D. A. Agard, MotionCor2: Anisotropic correction of beam-induced motion for improved cryo-electron microscopy. *Nat. Methods* **14**, 331–332 (2017). doi:10.1038/nmeth.4193 Medline

41. A. Rohou, N. Grigorieff, CTFFIND4: Fast and accurate defocus estimation from electron micrographs. *J. Struct. Biol.* **192**, 216–221 (2015). doi:10.1016/j.jsb.2015.08.008 Medline

42. S. H. Scheres, RELION: Implementation of a Bayesian approach to cryo-EM structure determination. *J. Struct. Biol.* **180**, 519–530 (2012). doi:10.1016/j.jsb.2012.09.006 Medline

43. T. Grant, A. Rohou, N. Grigorieff, *cis*TEM, user-friendly software for single-particle image processing. *eLife* **7**, e35383 (2018). doi:10.7554/eLife.35383 Medline

44. A. Kucukelbir, F. J. Sigworth, H. D. Tagare, Quantifying the local resolution of cryo-EM density maps. *Nat. Methods* **11**, 63–65 (2014). doi:10.1038/nmeth.2727 Medline

45. M. Biasini, S. Bienert, A. Waterhouse, K. Arnold, G. Studer, T. Schmidt, F. Kiefer, T. Gallo Cassarino, M. Bertoni, L. Bordoli, T. Schwede, SWISS-MODEL: Modelling protein tertiary and quaternary structure using evolutionary information. *Nucleic Acids Res.* **42**, W252–W258 (2014). doi:10.1093/nar/gku340 Medline

46. E. F. Pettersen, T. D. Goddard, C. C. Huang, G. S. Couch, D. M. Greenblatt, E. C. Meng, T. E. Ferrin, UCSF Chimera—A visualization system for exploratory research and analysis. *J. Comput. Chem.* **25**, 1605–1612 (2004). doi:10.1002/jcc.20084 Medline

47. R. Y. Wang, Y. Song, B. A. Barad, Y. Cheng, J. S. Fraser, F. DiMaio, Automated structure refinement of macromolecular assemblies from cryo-EM maps using Rosetta. *eLife* **5**, e17219 (2016). doi:10.7554/eLife.17219 Medline

48. P. Emsley, K. Cowtan, Coot: Model-building tools for molecular graphics. *Acta Crystallogr. D Biol. Crystallogr.* **60**, 2126–2132 (2004). doi:10.1107/S0907444904019158 Medline

49. P. D. Adams, P. V. Afonine, G. Bunkóczi, V. B. Chen, I. W. Davis, N. Echols, J. J. Headd, L.-W. Hung, G. J. Kapral, R. W. Grosse-Kunstleve, A. J. McCoy, N. W. Moriarty, R. Oeffner, R. J. Read, D. C. Richardson, J. S. Richardson, T. C. Terwilliger, P. H. Zwart, PHENIX: A comprehensive Python-based system for macromolecular structure solution. *Acta Crystallogr. D Biol. Crystallogr.* **66**, 213–221 (2010). doi:10.1107/S0907444909052925 Medline

50. W. L. Delano, The PyMol Molecular Graphics System (2002).

51. L. Wang, Y. Nam, A. K. Lee, C. Yu, K. Roth, C. Chen, E. M. Ransey, P. Sliz, LIN28 zinc knuckle domain is required and sufficient to induce let-7 oligouridylation. *Cell Reports* **18**, 2664–2675 (2017). doi:10.1016/j.celrep.2017.02.044 Medline